https://doi.org/10.5194/esd-2023-15
Preprint. Discussion started: 12 May 2023

Earth System Dynamics Discussions

Multi-centennial evolution of the climate response and deep ocean heat uptake in a set of abrupt stabilization scenarios with EC-Earth3

Federico Fabiano[1], Paolo Davini[2], Virna Meccia[1], Giuseppe Zappa[1], Alessio Bellucci[1], Valerio Lembo[1], Katinka Bellomo[2, 3], and Susanna Corti[1]

[1]Institute of Atmospheric Sciences and Climate (CNR-ISAC), Bologna (Italia)
[2]Institute of Atmospheric Sciences and Climate (CNR-ISAC), Torino (Italia)
[3]Polytechnic University of Turin, Department of Environment, Land and Infrastructure Engineering, Torino (Italia)

Correspondence: Federico Fabiano (f.fabiano@isac.cnr.it)

Abstract. Understanding long-term committed climate change due to anthropogenic forcing is key to inform climate policies, yet these timescales are still under-explored. We present here a set of 1000-year long *abrupt stabilization* simulations performed with EC-Earth3. Each simulation follows a sudden stabilization of the external forcing at the level specified by CMIP6 for historical (1990) or SSP5-8.5 scenario (2025, 2050, 2065, 2080, 2100) conditions, with a final temperature increase ranging between 1.4 and 9.6 K with respect to the pre-industrial baseline. Remarkably, the simulation stabilized at a level of greenhouse gases (GHGs) close to present-day (2025) well exceeds in the long term the Paris agreement goals of 1.5 and 2 degrees warming above pre-industrial, and only the 1990 simulation leads to a stabilized climate below 1.5 degrees warming. We first focus on the evolution of the climate response at multi-centennial timescales and its dependence on the level of forcing. Surface warming patterns evolve during the course of the simulations, with the most striking feature being a drastic acceleration of the warming in the Southern Ocean. The patterns of precipitation change also evolve during the stabilization runs: the drying trends found in the sub-tropical oceans and in Mediterranean-like hotspots in the SSP5-8.5 scenario tend to reduce, or even to reverse. We finally focus on the rate of heat storage in the global ocean, which is the main driver of the climate response at multi-centennial timescales. We find that the rate of warming of the deep ocean is almost independent from the amplitude of the forcing, so that most of the additional heat remains in the upper layers at high forcing. We hypothesize that this is due - at least partly - to a decreased ventilation of the deep ocean, caused by changes in the meridional overturning circulation (MOC). The results highlight the importance of studying multi-centennial timescales of climate change to better understand the response of the deep ocean, which will play a crucial role in determining the final state of the climate system once GHGs concentrations are stabilized.

1 Introduction

One of the main research topics in climate change studies regards the projection of the future state of the climate under different scenarios of anthropogenic greenhouse gases (GHG) and aerosol emissions. This activity is coordinated globally by

https://doi.org/10.5194/esd-2023-15
Preprint. Discussion started: 12 May 2023


Earth System Dynamics Discussions

the Coupled Model Intercomparison Project (CMIP) initiative (now at phase 6: Eyring et al., 2016), which defines a set of common protocols for both historical/future and idealized climate model simulations. On top of DECK integrations, which include the pre-industrial control and the abrupt-4xCO2 runs, an important piece of CMIP6 is represented by the historical simulations, based on the observed concentrations of GHGs and anthropogenic/natural aerosols, and the scenario simulations (ScenarioMIP), forced with a set of prescribed GHG and aerosol concentration scenarios for the XXI century (O'Neill et al., 2016; Gidden et al., 2019).

The scenario simulations allow us to assess the response of the climate system to different emission pathways for the next century and, as such, are a fundamental tool for informing climate policies and impact studies. However, one limitation is that these are transient simulations, in which the external forcing is continuously varying and the climate system - while rapidly changing - is not able to catch up with the new forcing and remains far from the equilibrium. In this respect, one fundamental question remains unanswered: which will be the equilibrium state of the climate once all of the warming linked to a specific level of forcing is realized? Tackling the problem with state-of-the-art climate models is challenging, due to their high computational cost and considering that the complete stabilization of the climate system would require centuries or even millennia for slower components (e.g. Li et al., 2013). Nevertheless, exploring the *final result* of the anthropogenic perturbation to the climate system is fundamental to assess the potential for irreversible changes associated with ice sheets/glaciers melting, sea-level rise and other tipping elements (Lenton et al., 2019; Armstrong McKay et al., 2022).

Also, much of the discussion about climate feedbacks and equilibrium climate sensitivity does not fully account for the response of slower components such as the deep ocean, but there is indication that inter-model differences in the rate of heat transfer to the deep ocean are a key factor in driving the spread in the surface response between models (Boé et al., 2009; Kostov et al., 2014; Gjermundsen et al., 2021; Bellomo et al., 2021). Due to the computational constraint, multi-centennial timescales have been mostly explored with EBMs (Energy Balance Models) or intermediate complexity models (e.g. Zickfeld et al., 2013). However, a few very long integrations with complex coupled GCMs (General Circulation Models) have also been performed to date. One remarkable example is the work by Li et al. (2013), who performed a 5000 years experiment with abrupt $4xCO_2$ forcing to achieve a complete stabilization in the deep ocean and analyse the equilibrium response of the ECHAM5/MPIOM model. More recently, the LongRunMIP protocol (Rugenstein et al., 2019) collected a multi-model ensemble of 1000-yr long climate simulations, most of which follow an abrupt doubling or quadrupling of the CO_2 concentration.

We here present a set of simulations performed with EC-Earth3, a state-of-the-art GCM participating to CMIP6 (Döscher et al., 2022), that also focus on multi-centennial timescales but following a different set-up with respect to LongRunMIP. Instead of an abrupt increase in CO_2 from the pre-industrial (PI) climate, each simulation features an *abrupt stabilization* of GHGs and aerosols concentrations. Specifically, each simulation is branched at a specific year from the CMIP6 historical or the SSP5-8.5 simulation and the GHGs and aerosol concentrations are kept fixed thereafter at the branching-year level. The final states represent the world we would have in the far future if the atmospheric concentration of GHGs and aerosols were suddenly stabilized. Of course this is different from a sudden cease in emissions, since we do not here consider chemistry and carbon-cycle feedbacks (see for example the ZECMIP protocol, Jones et al., 2019).

https://doi.org/10.5194/esd-2023-15
Preprint. Discussion started: 12 May 2023

Earth System Dynamics Discussions

The main aim of this study is to explore the long-term pathway towards stabilization of the climate system, with a focus on the evolution of the patterns of temperature and precipitation and on the response of the deep ocean. The paper is structured as follows: Section 2.1 presents the model and the simulation set-up; Section 3.1 gives a general overview of some standard indices; Section 3.2 focuses on the patterns of warming and precipitation change at long timescales; Section 4 analyses the response of the deep ocean.

2 Data and methods

2.1 Model and simulation set-up

The simulations have been performed with the EC-Earth3 climate model (version 3.3.3), a state-of-the- art Earth-system model, which is developed by a consortium of European research institutions (Döscher et al., 2022). EC-Earth3 includes robust and validated components for the atmosphere (the ECMWF IFS model cy36r4), the ocean (NEMO 3.6; Madec, 2008), the sea ice (LIM3; Fichefet and Maqueda, 1997) and land processes (H-Tessel; Balsamo et al., 2009). It is worth to note that v3.3.3 is the same version used for the CMIP6 inter-comparison project. The model has been used in the standard CMIP6 resolution TL255L91-ORCA1L75, corresponding to a horizontal resolution of approximately 80 km and 100 km in the atmosphere and the ocean, respectively. In the vertical, the atmosphere uses 91 levels (up to 1 hPa) and the ocean 75 levels.

Each stabilization run lasts 1000 years and is branched from the corresponding CMIP6 simulation (historical/SSP5-8.5) of EC-Earth3 (r4i1p1f1 member), following an abrupt stabilization of the GHG concentrations and of the aerosol forcing. We run a set of six simulations, corresponding to 1990 (historical), 2025, 2050, 2065, 2080 and 2100 (SSP5-8.5) conditions. In the following, we refer to a specific simulation as "b###" with the hashes referring to the last three digits of the year of branching (i.e. "b100" for the 2100 simulation). GHG concentrations are those provided as standard input for CMIP6 (see https://esgf-node.llnl.gov/projects/input4mips/). Aerosol forcing is prescribed as optical depth following the MACv2-SP interpretation of the historical period (Stevens et al., 2017) and future CMIP6 scenarios (Fiedler et al., 2019). In terms of CO_2 concentrations, the six simulations correspond roughly to 1.25, 1.5, 2, 2.5, 3 and 4 times the pre-industrial value. The exact concentrations of CO_2, CH_4 and N_2O are shown in Table 1. Aerosol forcing also differs between the simulations, since the SSP5-8.5 scenario assumes that aerosol emissions will evolve during the XXI century: the main trends being a steady decrease over East Asia and an increase followed by a decrease over India and Africa, peaking in 2040 and 2080 respectively (see bottom right panel of Fig. 3 in Fiedler et al., 2019).

As most current generation GCMs, this model version does not include a proper treatment of Greenland and Antarctic ice sheets. In fact, these are represented as mountains (with fixed orography), which are covered by a 10 meter water-equivalent amount of snow. The snowfall exceeding this threshold is directly distributed as runoff to the ocean around Greenland/Antarctica, to ensure water conservation. This works quite well in a pre-industrial or present-day climate or in short scenario simulations. In our simulations, however, this simplistic representation results in a complete melting of the snow cover over Greenland and parts of Antarctica at high forcing after a few centuries, which are then left as mountains covered by bare soil. This is of

https://doi.org/10.5194/esd-2023-15
Preprint. Discussion started: 12 May 2023


Earth System Dynamics Discussions
Open Access
EGU

Table 1. Values of GHGs for all simulations.

	PI	b990	b025	b050	b065	b080	b100
CO_2 (x PI)	1	1.25	1.5	2	2.5	3	4
CO_2 (ppm)	284	354	432	563	691	864	1135
CH_4 (ppb)	808	1717	1954	2446	2651	2652	2415
N_2O (ppb)	273	309	336	358	370	380	392

course unrealistic and drives a strong local surface warming in Greenland and Antarctica in the high forcing simulations (in particular in b100), which should then be interpreted accordingly.

2.2 Definitions and procedures

In this Section, we provide definitions and detail the methods used throughout the paper. The variables considered are part of standard CMIP6 output for the atmospheric (2-meter air temperature, precipitation, shortwave (SW) and longwave (LW) radiation at top-of-atmosphere (TOA), net TOA flux $N = SW_{in} - SW_{out} - LW_{out}$) and ocean component (sea-ice concentration, 3D conservative temperature, overturning mass streamfunction).

Stabilization timescale

The duration of the surface temperature stabilization is estimated in Section 3.1 (Table 2) through a series of Mann-Kendall (MK) trend tests, with the following iterative procedure:

1. an MK test is performed from y_0 to the end of the simulation, starting from $y_0 = 0$;
2. if the test indicates a significant increasing trend, y_0 is moved forward by 10 years and step 1 repeated;
3. if the test indicates an insignificant trend or a significant decreasing trend, y_0 is taken as the estimate of the stabilization period.

If condition 3 is not satisfied and $y_0 > 950$ years, then no estimation of the stabilization is given, since the remaining time is too short to assess a trend (this is the case of b050 in Table 2). Considering the estimates in Table 2 for the surface stabilization, we refer throughout the paper to timescales of the order of the stabilization period (multi-centennial) as "long" or "stabilization" timescales, and at shorter timescales, up to one century, as "short" or "transient" timescales.

Temperature/Precipitation patterns

The temperature patterns discussed in Section 3.2 (Figure 6) are calculated as a linear regression of the local surface temperature against the 50-year lowpass-filtered global mean 2-meter air temperature (GTAS), using the whole time range of the simulations. The GTAS is lowpass-filtered to highlight the long-term patterns of change rather than the interannual and decadal

https://doi.org/10.5194/esd-2023-15
Preprint. Discussion started: 12 May 2023


Earth System Dynamics Discussions

variability patterns (in particular the ENSO pattern), which can be of the same or higher order of magnitude for low warming scenarios. Precipitation patterns in (Figure 7) are calculated in an analogous way, apart from the fact that the local precipitation field is first divided by the local pre-industrial mean field to obtain the relative precipitation. The precipitation pattern is masked where the pre-industrial average total annual precipitation is less than 50 mm/year, to avoid over-emphasizing changes in desert areas. The significance of the changes is assessed through a Wald test.

We stress here that, for the stabilization simulations, the trends are calculated starting from the stabilization year, and thus don't include changes happened before branching, during the transient SSP5-8.5 simulation. This is done to highlight how the patterns evolve during the stabilization with respect to the transient SSP5-8.5 simulation. Therefore, the interpretation should be careful, for example, regarding the inversion of the precipitation trends (Figure 7): in most cases, the stabilization trend can locally reduce the transient response, but the amplitude is generally not enough to reverse the sign of the total change with respect to pre-industrial.

Ocean Heat Content

We calculated the additional heat stored in an ocean layer between z_1 and z_2 as:

$$\Delta H_{12} = \sum_{z_1}^{z_2} c_p \int_{A_z} m_A \Delta\Theta_c \, dA$$

where $\Delta\Theta_c$ is the change in conservative temperature (McDougall, 2003) with respect to pre-industrial, c_p is the specific heat capacity, A_z is the area covered by level z and m_A the mass per unit area of that level. The conservative temperature is usually very similar to the potential temperature, and indistinguishable for most purposes. However, the former is more indicated for heat budget analysis (McDougall, 2003). Since the simulations are branched from the r4i1p1f1 member of the CMIP6 SSP5-8.5 simulation, which derives from the r4 member of the CMIP6 historical, the pre-industrial state is taken as the 50 years that anticipate the branching of the r4 historical simulation.

Meridional Overturning Circulation indices

The streamfunctions of the Meridional Overturning Circulation for the global, Atlantic and Pacific/Indian oceans are available as model outputs. We define here the Atlantic MOC (AMOC) index as the maximum of the Atlantic MOC streamfunction between 30 and 50 N and 500 and 2000 m depth. The abyssal Southern MOC (SMOC) index is defined here as the average value of the global MOC streamfunction between 30 and 50 S and 3000 to 4000 m depth. The average is taken rather than the maximum to reduce the fluctuations in the index.

https://doi.org/10.5194/esd-2023-15
Preprint. Discussion started: 12 May 2023

Earth System Dynamics Discussions
Open Access
EGU

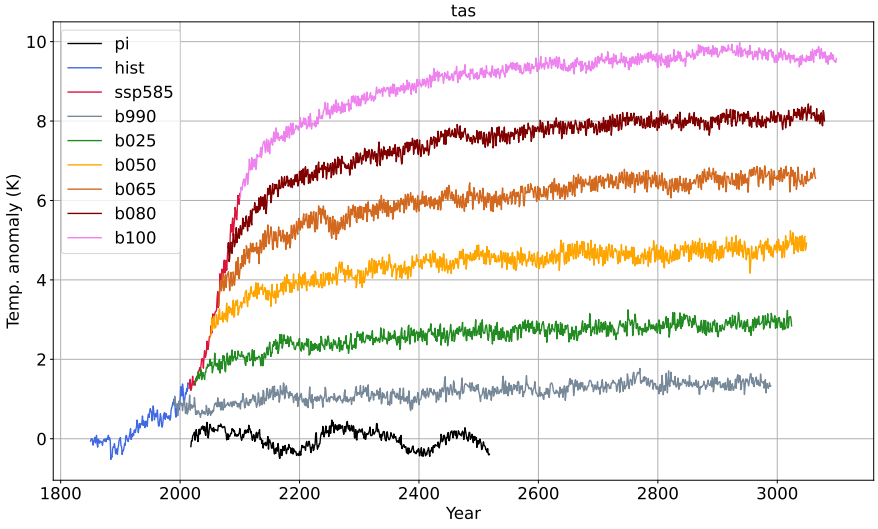

Figure 1. Global mean surface air temperature (GTAS) anomaly of the historical (hist), SSP5-8.5, b990, b025, b050, b065, b080 and b100 with respect to the pre-industrial mean climate.

3 Results

3.1 Overview

We give here a general overview of the simulations, analysing the global mean response to different levels of stabilized forcing. Figure 1 shows the GTAS anomaly with respect to the pre-industrial climate for the six runs. The warming continues in all experiments well after the abrupt stabilization of the GHG concentrations, and the final anomaly ranges between 1.4 to 9.6 K above the pre-industrial mean climate. Values for each experiment are indicated in Table 2. Even the relatively low forcing b025 simulation well exceeds in the long term the Paris agreement goals of 1.5 and 2 degrees warming above pre-industrial, while b990 would represent the only stabilized climate consistent with those goals. As a first estimate, this shows that, for the EC-Earth model, the target CO_2 concentration in the atmosphere needed to land in a desirable stabilized climate is much lower than the scenario concentration for 2025 (432 ppm), and very close to the 1990 concentration (354 ppm). Apparent from Figure 1, it is the centennial oscillation in the pre-industrial temperature (black line), which is driven by internal variability of the Atlantic Meridional Overturning Circulation (AMOC) (Meccia et al., 2022). Also the stabilization simulations feature internal variability in GTAS at multi-decadal timescales, but with relatively smaller amplitude and period (see Meccia et al. (2022) for a discussion of the AMOC variability in b050).

An estimate of the timescale for the stabilization of the surface climate is given in Table 2 by applying the Mann-Kendall test to the GTAS timeseries (details on the method can be found in Section 2.2). The global mean surface temperature stabilizes

https://doi.org/10.5194/esd-2023-15
Preprint. Discussion started: 12 May 2023

in most cases before the end of the simulation, with the notable exception of b050, which still has a significant positive trend at the end. Another way to look at the residual changes at the surface is through the residual increase in GTAS in the last 500 years, which is of the order of a few tenths of a degree for all simulations. Interestingly, despite the extreme forcing, the b100 simulation has the shortest surface stabilization period (even shorter than b990), and features a residual temperature increase in the last 500 years which is less than that in the intermediate b050, b065 and b080 simulations.

Table 2. Total ΔGTAS at the end of the simulation with respect to pre-industrial, ΔGTAS of last 500 years, final net TOA flux (considering 30-year periods) and estimated surface stabilization period (see Section 2.2).

	b990	b025	b050	b065	b080	b100
ΔGTAS (K) (final)	1.4	2.9	4.9	6.6	8.1	9.6
ΔGTAS (K) (last 500)	0.1	0.2	0.4	0.5	0.5	0.3
net TOA (W/m^2)	0.09	0.14	0.07	0.12	-0.06	-0.12
surface stabilization (years)	690	780	-	800	910	650

Figure 2 shows the annual global mean precipitation against GTAS for all runs. The trend is close to linear during the transient SSP5-8.5 simulation, as shown by the linear fit to the red dots in Figure 2 (left panel). An apparent feature of the stabilization simulations is an intensification of the hydrological cycle with respect to the transient response, implying more precipitation for the same global warming level. This is likely due to a larger weakening of the hydrological cycle in the SSP5-8.5 scenario due the rapid adjustments to GHG forcing, whose response scales with GHG concentrations rather than with surface mean temperature (Samset et al., 2016). Indeed, the transient SSP5-8.5 simulation shows a precipitation increase of about 1.9% per 1 K of global warming, slightly larger than the 1.7%/K trend during the historical period (right panel of Figure 2). The stabilization runs all show larger trends, from 2.2 to 2.5% per degree of warming.

Figure 3 shows the winter and summer sea-ice extent for the Arctic (upper panels) and for the Antarctic region (bottom). Arctic winter sea-ice extent decreases progressively in all simulations, stabilizing towards the end of the period for most runs, with the notable exception of b065. b100 simulates an abrupt collapse just a few years after the branch-off from SSP5-8.5: this behaviour has already been observed in an extended RCP8.5 scenario in a previous version of EC-Earth (Meccia et al., 2020) and in other climate models (Bathiany et al., 2016; Drijfhout et al., 2015). b065 has apparently reached a tipping point in the winter Arctic sea-ice and features a strong instability in the whole simulation, switching periodically from a low to a high ice cover state. In summer, the Arctic reaches a completely ice-free state in all simulations shortly after the branch-off, except for b990 and b025. The latter also shows an almost complete collapse, although with significant interannual variability. Only b990 retains a considerable fraction of Arctic summer sea-ice. Antarctic sea-ice experiences a gradual summer decline in b990 and b025, while all other simulations reach a completely ice-free state during the transient or at the beginning of the stabilization period. As for the summer Arctic sea-ice, eventually b025 also shows an almost complete collapse of summer Antarctic sea-ice cover. The winter Antarctic sea-ice cover experiences a gradual decline during the course of all simulations, reflecting the delayed warming of the Southern ocean. b080 and b100 eventually reach an ice-free state, b050 and b065 stabilize in the

https://doi.org/10.5194/esd-2023-15
Preprint. Discussion started: 12 May 2023

Earth System Dynamics
Discussions
Open Access
EGU

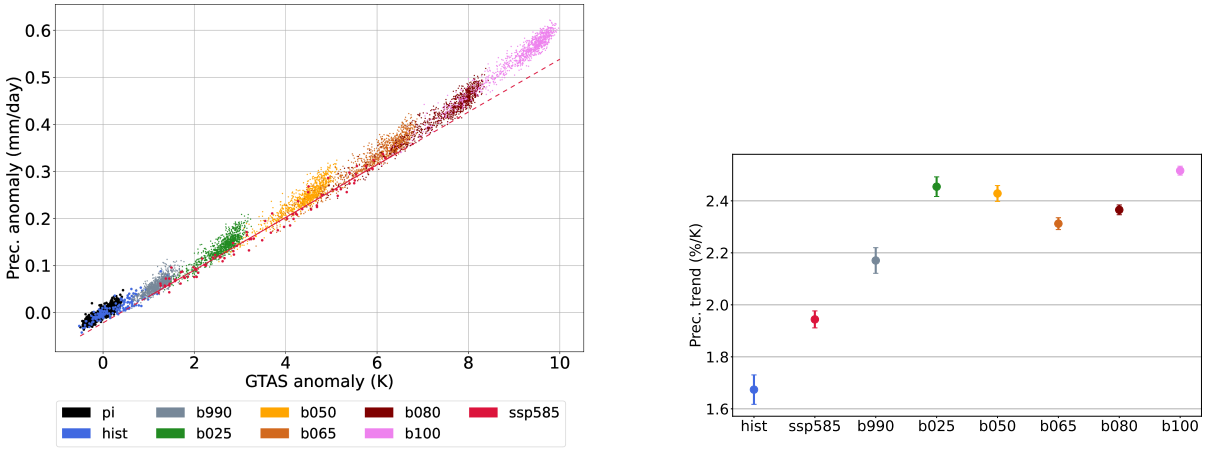

Figure 2. Left panel: Global annual mean precipitation anomaly with respect to the GTAS anomaly with respect to pre-industrial. The red line is a linear fit to the SSP5-8.5 data. Right panel: trend of the global annual-mean relative precipitation change with respect to GTAS for each simulation.

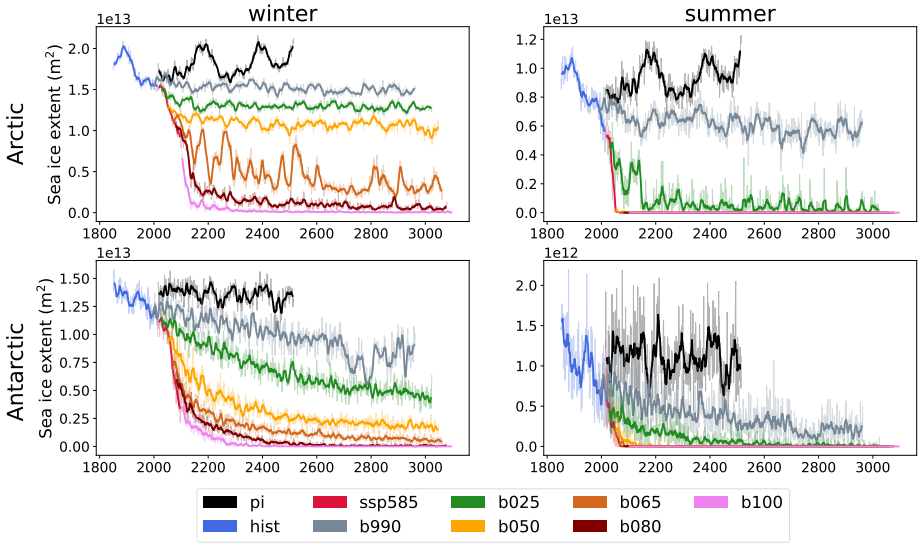

Figure 3. Upper panels: Arctic sea-ice extent at the end of the local winter (March) and summer (September) seasons. Bottom panels: Antarctic sea-ice extent at the end of the local winter (September) and summer (March) seasons. The thin lines show the monthly mean values, the thick ones are 10-year running means.

https://doi.org/10.5194/esd-2023-15
Preprint. Discussion started: 12 May 2023

Earth System Dynamics
Discussions
Open Access
EGU

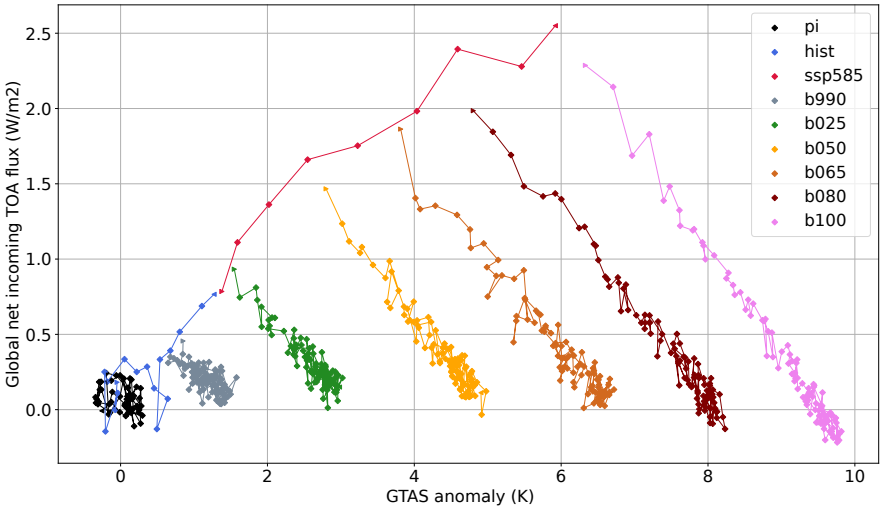

Figure 4. Global net energy imbalance at TOA vs GTAS anomaly of the different simulations. Dots represent 10-year averages.

second half of the simulation retaining a small fraction of the original sea-ice cover, while b990 and b025 are still drifting towards their new equilibrium at the end of the simulation.

The path to equilibrium of the simulations can be appreciated in Figure 4, which shows a scatterplot of the global net energy imbalance at TOA (W/m^2) with respect to GTAS, averaged every 10 years. The imbalance ranges initially from about 0.5 W/m^2 for b990 to about 2.5 W/m^2 for b100, and then slowly approaches zero during the course of the simulation. In this respect, the stabilization scenarios are radically different from SSP5-8.5 and other transient future scenarios, which feature instead an increasing energy imbalance at TOA (shown by the red dots/line in Figure 4). The global mean response of the system is close to linear at multi-centennial timescales, although we are missing here Earth-system feedbacks related to land-ice and vegetation which would matter at these timescales (see e.g. Knutti et al. (2017)). A slightly negative value of net TOA at complete equilibrium is to be expected, since the IFS model presents a spurious internal energy production of about 0.2 W/m^2 (Döscher et al., 2022). Interestingly, b100 gets closer to TOA energy balance at the end of the period than all other simulations, and this is consistent with the estimate of the surface stabilization period (Table 2).

3.2 Long-term evolution of temperature and precipitation patterns

We now analyze the spatial patterns of change in the stabilization simulations. Figure 5 shows the final surface temperature anomaly (last 30-years) for each simulation with respect to the pre-industrial climate. Historical and SSP5-8.5 simulations are also shown for comparison. The analogous maps of final change for precipitation are shown in the supplementary Figure S1.

https://doi.org/10.5194/esd-2023-15
Preprint. Discussion started: 12 May 2023

Earth System Dynamics
Discussions
Open Access
EGU

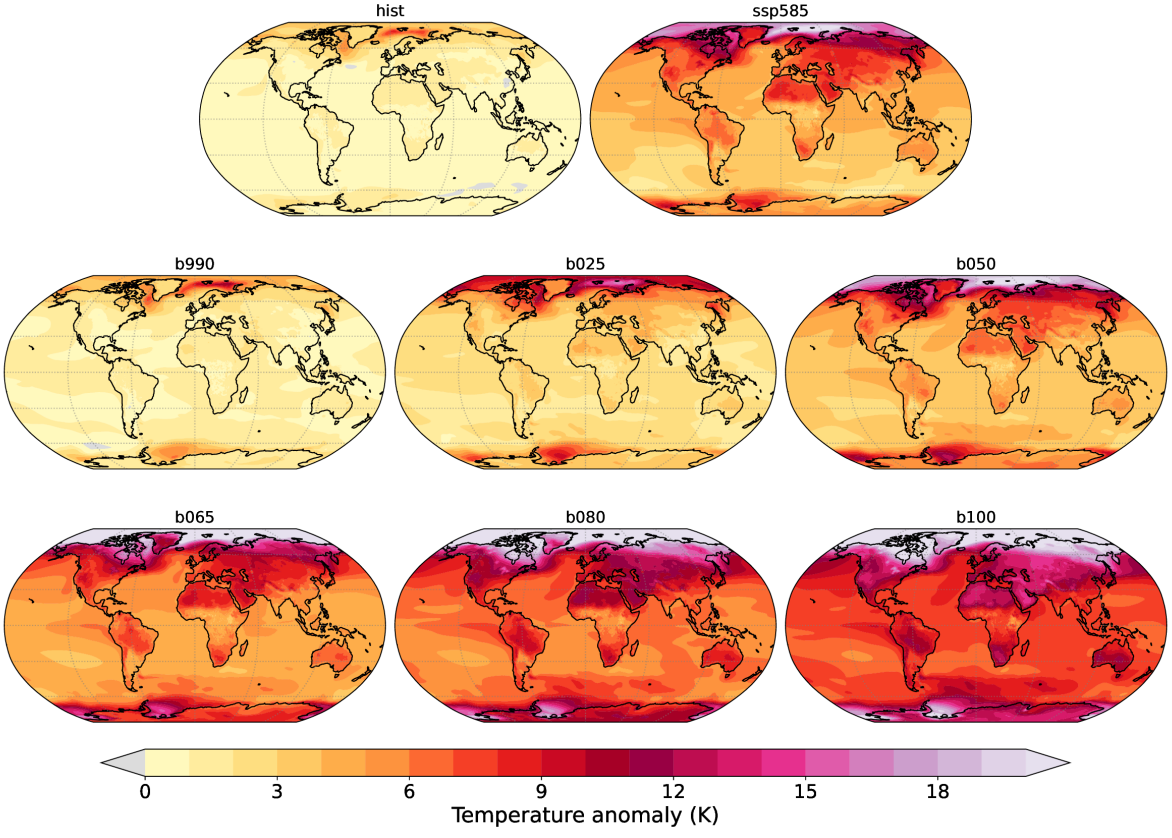

Figure 5. Temperature anomaly with respect to PI climate at the end of each simulation (30 yr mean).

To assess in which respect the stabilization trends differ from the transient ones, we computed warming patterns (local temperature change per degree of global warming) for all simulations, as described in Section 2.2. The complete set is shown in Figure S2, and we show in Figure 6 (top row) only the SSP5-8.5, b025 and b100 patterns. The bottom row of Figure 6 shows instead the ratio of the stabilization warming patterns to the transient one, to better highlight the differences. As expected, the patterns differ in various respects between the transient and stabilization simulations. First, the SSP5-8.5 simulation features a strong asymmetry of warming between land and oceans, which is still present but much reduced in b025 and almost disappeared in b100 (apart from the northernmost regions of America and Siberia). This is well known and due to the larger thermal inertia of the water mass with respect to the land surface (King et al., 2020; Lee et al., 2021).

Another difference regards the intensity and extent of the amplification at the extreme northern latitudes. If b025 still features a strong Arctic amplification, similar to the SSP5-8.5 one, this is much reduced in b100, since most of the warming there already took place during the transient. In fact, as seen in Figure 3, both the Arctic and Antarctic sea-ice cover keep reducing during b025, while b100 is already almost sea-ice-free shortly after the beginning. The extreme inland warming of Greenland in b100

https://doi.org/10.5194/esd-2023-15
Preprint. Discussion started: 12 May 2023

Earth System Dynamics
Discussions
Open Access
EGU

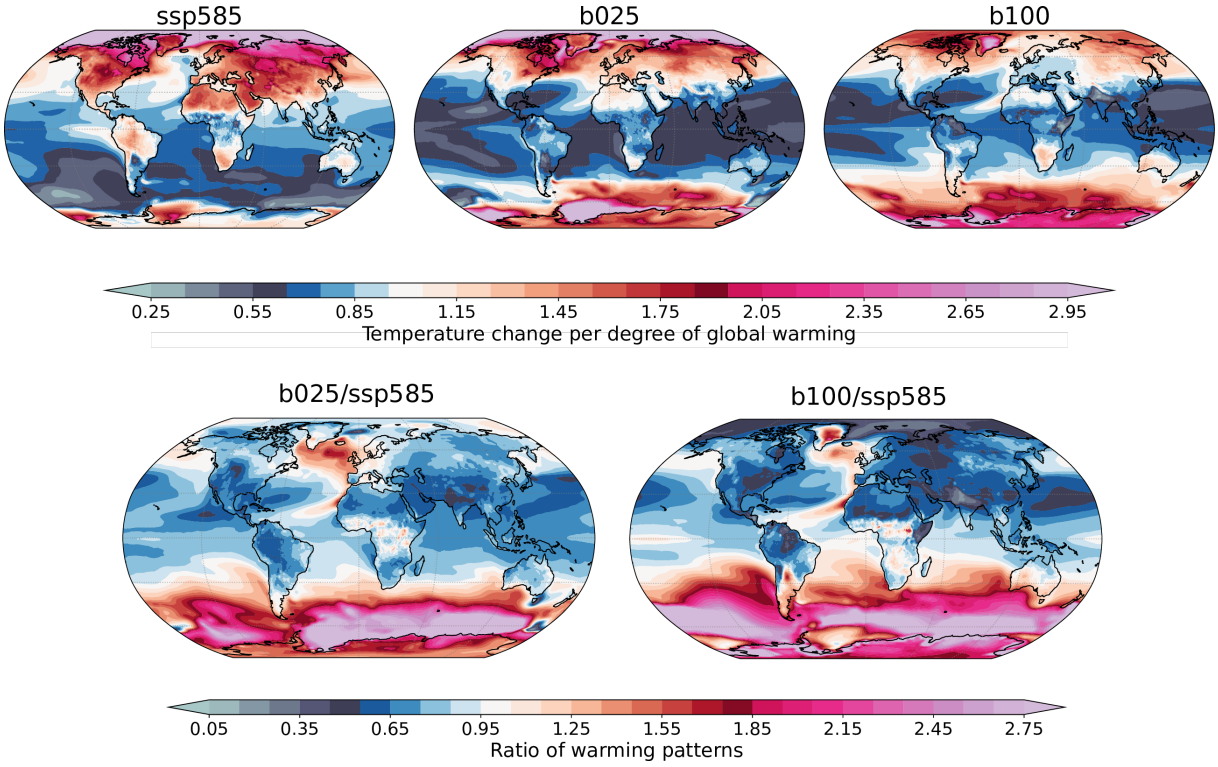

Figure 6. Top row: local surface temperature change per degree of global warming during the course of the simulation, for SSP5-8.5, b025 and b100. A value smaller (larger) than one means that the local rate of warming is slower (faster) than the global mean. All trends are significant at the 95% level. Bottom row: ratio of the stabilization warming patterns (b025, b100) to the transient one (SSP5-8.5).

is spurious, since the model does not include a proper land-ice component, as explained in Section 2.1. The North Atlantic subpolar gyre also shows an interesting behaviour, with an intensified warming during stabilization, more evident in b025 (Figure 6, bottom row), and likely linked to the recovery of the AMOC (see Figure 12).

The most striking difference is in the Southern Hemisphere, which lags the global warming during the SSP5-8.5 simulation, due to the upwelling of cold waters in the Southern Ocean (Armour et al., 2016). The warming trend in the Southern Ocean drastically increases at longer timescales, being first mostly concentrated to the South of the Atlantic and Indian oceans at low warming (b025) and then extending to the Pacific region as well (b100). The increased warming in b100 also shifts northwards, reaching inland Southern South America and Australia. As for Greenland, also the inland warming of Antarctica in b100 is unreliable due to the lack of a land-ice component. As a consequence of the increased warming in the Southern hemisphere and decreased warming in the Northern one, the global warming pattern is progressively more symmetric in the North-South direction across the stabilization runs. The region with minimum trend moves accordingly from the Southern ocean in the transient simulation to the tropical and sub-tropical oceans.

https://doi.org/10.5194/esd-2023-15
Preprint. Discussion started: 12 May 2023

Earth System Dynamics
Discussions
Open Access
EGU

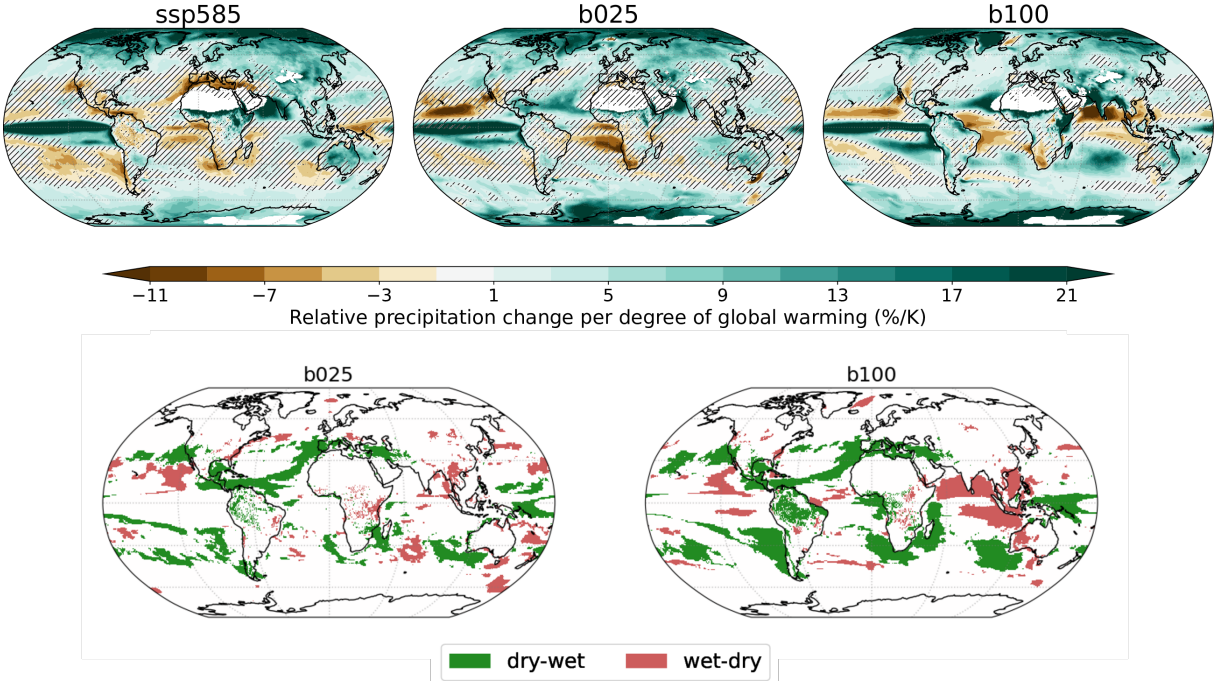

Figure 7. Top row: relative precipitation change per degree of global warming during the course of the simulation, for SSP5-8.5, b025 and b100. Hatching indicates regions where the trends are not significant at the 95% level. Bottom row: regions where the sign of the precipitation trend reverses during stabilization (b025/b100) with respect to the transient (SSP5-8.5) are highlighted. Dry-wet transition is shown in green, wet-dry in red. Regions with less than 50 mm/year in the pre-industrial climate are masked.

We now focus on the evolution of precipitation patterns during stabilization. Figure 7 shows the pattern of relative precipitation change per degree of global warming (top row) for SSP5-8.5, b025 and b100 (the other simulations are shown in Figure S3). Regional trends differ significantly between the transient and stabilization simulations, also changing sign in some cases. The bottom row of Figure 7 highlights regions that turn from a drying trend during SSP5-8.5 to a wettening during stabilization (green) and the opposite condition (wettening → drying, in red). For the highlighted regions, the final change with respect to the pre-industrial climate is partially mitigated and less severe than at the beginning of the simulations. However, the stabilization change is usually smaller than the transient one and the sign of the total change with respect to pre-industrial is generally consistent with that of the transient response (see Figure S1). Drying trends found in the sub-tropical oceans and in Mediterranean-like hotspots during transient tend to reduce during stabilization, or even to reverse. This is particularly clear for the subtropical North-Atlantic and central America, which experience drying during SSP5-8.5 and wettening in b025 and b100, and also seen in the Mediterranean region, although the stabilization trends are not significant there. This long-term relaxation of the drying over the Mediterranean region was also observed for the ECP4.5 extended scenario of CMIP5, up to 2300 (Zappa et al., 2020).

https://doi.org/10.5194/esd-2023-15
Preprint. Discussion started: 12 May 2023

Earth System Dynamics Discussions

The South-eastern Pacific and the Pacific coast of South America also experience drying in the transient and partly in b025, but wettening in b100. Overall, this is also in line with Zappa et al. (2020), who found no trend over Chile in the extended ECP4.5 scenario. However, we observe that the long-term trend in the region is also partly dependent on the level of global warming. This is also true for the Southern sub-tropical oceans, namely the ocean around South Africa and off the south-western coast of Australia, that turn more markedly to wettening in b100. The changes are however mostly over the oceans in this case (He and Soden, 2017), with the inland drying in South Africa still going on in b025 and b100. b100 also shows a significant inversion of the drying trend over Amazonia, that turns to wettening, more pronounced in the western part. This is likely connected with global changes in the Walker circulation system, which also lead in b100 to increased wettening of the Horn of Africa and pronounced drying in the northern Indian ocean and in the South East Asian sea. The California peninsula also shows an inversion of the transient trends, that turn to wettening in the northern part (consistent with Zappa et al. (2020)) and drying in the southern pensinsula.

4 Response of the deep ocean

The long-term scales of climate stabilization are primarily driven by the ocean thermal inertia and by the efficiency of heat transfer towards the deeper layers of the ocean. Figure 8 shows the additional heat stored globally in three ocean layers: the upper layer down to 700 m depth, the mid layer from 700 to 2000 m and the deep layer below 2000 m. The contributions of the three layers are stacked one on top of the other, so that the cumulative curve shows the total heat absorbed by the global ocean during the course of the simulation. As expected, the total amount of heat stored is roughly proportional to the forcing strength, and it is still increasing at the end of the simulations in all cases. However, the rate at which the heat is stored in the three layers differs depending on the forcing. The mid and upper ocean layers show marked differences both in the amount and in the rate of heat storage. Specifically, the trend is roughly linear for the upper and intermediate ocean layers in b990 and b025, while an exponential relaxation behaviour is apparent in the simulations with larger forcing. Remarkably, the deep layer heat storage is pretty linear with time in all simulations and almost independent from the external forcing.

Table 3. Additional heat stored globally in upper, mid and deep ocean layers at the end of the simulations (30-yr averages, values are in units of $10^{24} J$).

Layer	b990	b025	b050	b065	b080	b100
Upper (< 700 m)	0.7	1.7	2.9	4.0	5.1	6.4
Mid (700-2000 m)	1.1	2.3	3.7	4.9	5.9	6.9
Deep (> 2000 m)	2.3	3.2	3.5	3.5	3.5	3.3
Total	4.1	7.2	10.1	12.5	14.4	16.6

In fact, the distribution of heat in the three layers is also strongly dependent on forcing. In particular, the larger the forcing, the larger the relative fraction of heat that remains in the two upper layers. This is summarized in Table 3, which shows the

https://doi.org/10.5194/esd-2023-15
Preprint. Discussion started: 12 May 2023

Earth System Dynamics
Discussions
Open Access
EGU

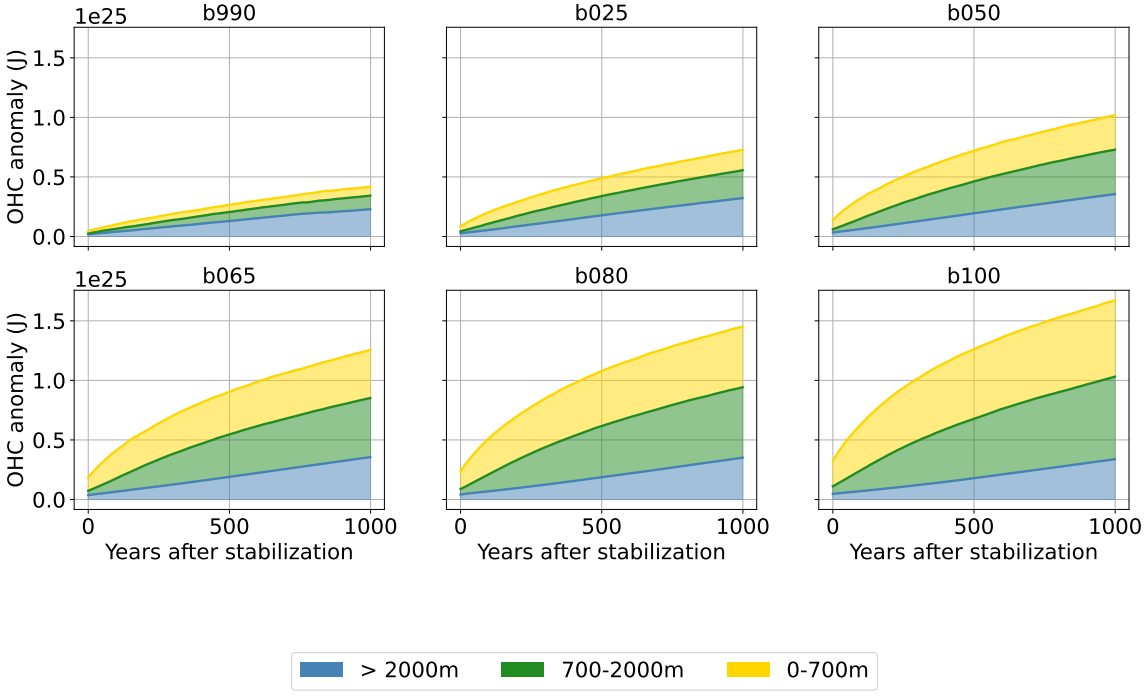

Figure 8. Cumulative values of global ocean heat content anomaly for all stabilization simulations in three depth regions: 0-700m, 700-2000m and below 2000m. The contributions of the three layers are stacked one on top of the other, so that the cumulative curve shows the total heat absorbed by the global ocean. The relative contributions of the three layers are shown in supplementary Figure S4.

heat content anomaly of each layer at the end of the run with respect to the pre-industrial climate, and in supplementary Figure S4, which is the analog of Figure 8 showing the relative contribution of each layer to the total OHC. When stabilizing at the 1990 forcing, more than half of the heat absorbed by the global oceans is transferred to the deepest layer in 1000 years. On the opposite, just about 20% of the additional oceanic heat is absorbed by the deep layer at the end of the b100 simulation. Apart from b990, the final heat content in the deep layer is in all cases between 3.2 and 3.5×10^{24}J, with a maximum for the intermediate forcing of b050 and b065. This despite the fact that, due to the simulation setup, the higher forcing cases had more time to accumulate heat in the deep ocean, since they started from later stages of the SSP5-8.5 simulation.

The final state of the ocean can be appreciated from Figure 9, which shows the global mean profile of the ocean temperature anomaly at depth with respect to the pre-industrial climate, both at the start (dotted) and end (solid) of the simulations. The b990 simulation appears to be quite close to final equilibrium, with an almost uniform distribution of the additional heat along the depth profile. The other simulations are instead increasingly away from a uniform redistribution of heat, in particular below 2000 m, with most of the heat still trapped in the surface layers for the extreme forcing cases. For comparison, the final equilibrium state of the deep ocean in the abrupt $4xCO_2$ experiment by Li et al. (2013), showed an almost uniform 8 K

https://doi.org/10.5194/esd-2023-15
Preprint. Discussion started: 12 May 2023

Earth System Dynamics
Discussions
Open Access
EGU

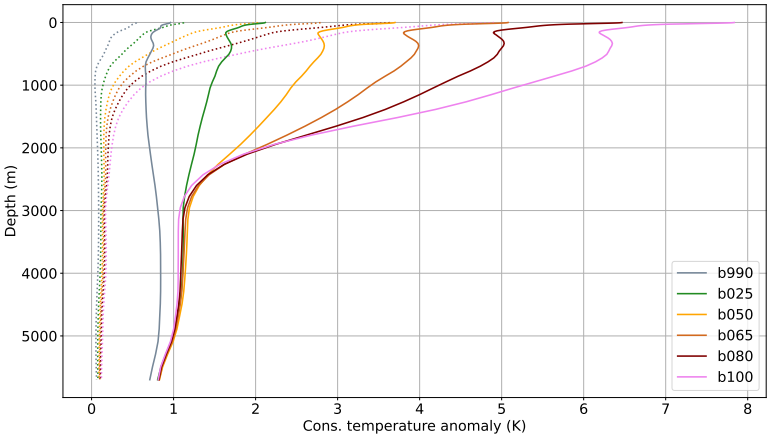

Figure 9. Global mean profile of the ocean temperature anomaly at depth with respect to the pre-industrial climate. The dotted lines represent the starting point of the simulations, the solid ones the final state. Shown are 30-yr averages, the conservative temperature variable has been used.

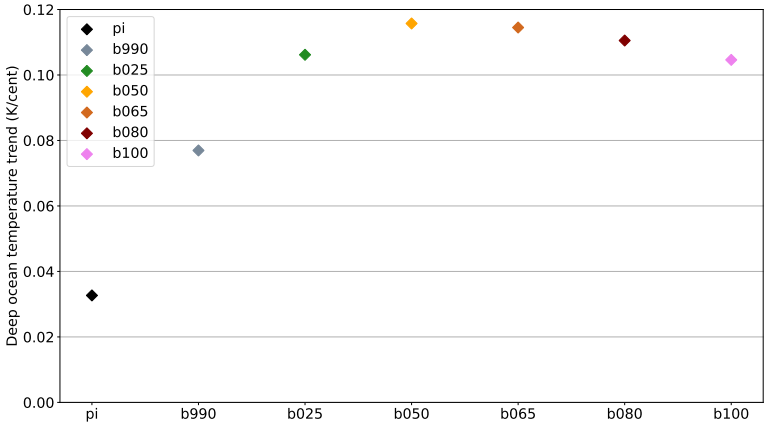

Figure 10. Linear trend (K/century) of the deep ocean mean temperature (at depths $>$ 2000 m) in all simulations and in the pre-industrial control.

temperature anomaly at depth after 5000 years. If the equilibrium state requires a uniform redistribution of heat at depth, at the current pace equilibrating the deep ocean will still take centuries for the low forcing b025 and millennia for b100.

The fact that the deep ocean heat uptake is largely independent from the external forcing was an unexpected finding. In particular, one would expect the rate of heat uptake to be larger for larger warming in the surface layers, through the advection

https://doi.org/10.5194/esd-2023-15
Preprint. Discussion started: 12 May 2023

Earth System Dynamics
Discussions
Open Access
EGU

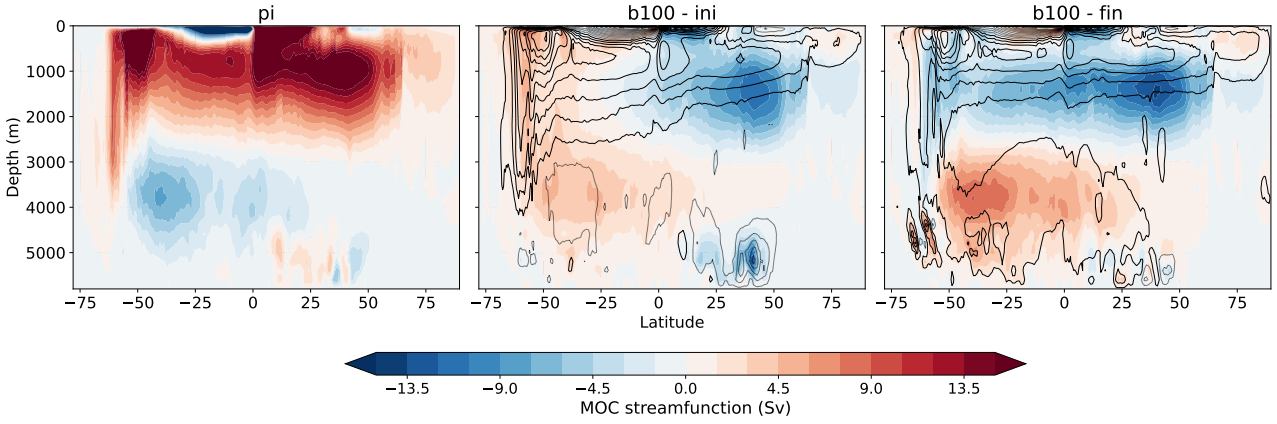

Figure 11. Global MOC streamfuction (Sv) for the average pre-industrial (shading, left panel), and the initial and final states of the b100 simulation (mid and right panel; shading: difference to PI, contour: full field at steps of 3 Sv).

of warmer surface waters. However, as shown in Figure 10, the trend in the deep ocean temperature does increase with forcing in b990, b025 and (slightly) b050, but then reaches an absolute maximum and starts to slowly decline up to b100. The drift (positive trend) in the pre-industrial deep ocean is a common feature of CMIP models and is mainly due to computational reasons, since the complete equilibration would require a multi-millennial spin-up simulation. The forced trend in b990 to b100 is however 3 to 4 times larger than that in the pre-industrial, proving that the deep ocean is indeed *feeling* the increased forcing.

The downward transfer of heat in the ocean is the result of the complex interplay between various processes (Gregory, 2000; Hieronymus and Nycander, 2013; Exarchou et al., 2015), namely: advection of heat (including both the resolved advection and the parametrized eddy advection in the model), dia- and isopycnal diffusion, vertical mixing (including wind mixing and convection). In the NEMO model, the pre-industrial equilibrium at depth is maintained by a balance between the geothermal heating at the bottom, the downward heat flux from diapycnal diffusion, and the upward heat flux from advection (resolved + eddy) and isopycnal diffusion (Hieronymus and Nycander, 2013). Interestingly, the resolved advection provides a downward heat flux, but the parametrized eddy-induced advection of heat is upward, resulting in a net upward flux (Hieronymus and Nycander, 2013). It is outside the scope of this paper to provide a complete budget of all the processes involved in the deep ocean warming, which would require either online diagnostics (Hieronymus and Nycander, 2013) or offline calculations to reproduce the model parametrizations (Exarchou et al., 2015). Nevertheless, we briefly discuss here the role of the heat advection by the resolved circulation.

We hypothesize that the reduced efficiency in the deep ocean heat uptake at larger forcing can be partly explained by a decrease in the downward heat advection to the intermediate and deep ocean layers, due to a reorganization of the global Meridional Overturning Circulation (MOC). Figure 11 shows the streamfunction of the global MOC for the average pre-industrial (left panel), and the initial and final states of the b100 simulation (mid and right panel). A strong damping of the

https://doi.org/10.5194/esd-2023-15
Preprint. Discussion started: 12 May 2023

upper MOC branch in the Northern hemisphere can already be appreciated at the beginning of b100 (Figure 11, middle panel), and is due to the well known reduction in the strength of the Atlantic MOC (AMOC) during SSP5-8.5 (e.g. Bellomo et al., 2021). The circulation in the Southern ocean is still quite unaffected or even strengthened at this stage. Interestingly, during the millennial b100 simulation, the damping of the MOC proceeds mostly at depth, producing a strong reduction of the circulation below 1000 m depth in the final state, particularly evident in the Southern ocean (Figure 11, right panel).

The changes observed for b100 are also seen in the other simulations, but their amplitude is amplified in the higher forcing cases. To better appreciate the behaviour of the upper and lower branches of the MOC in all simulations, we focus here on two indices, shown in Figure 12:

- the maximum of the Atlantic MOC (AMOC) between 30 and 50 N and 500 and 2000 m (Figure 12, left panel);
- the average value of the abyssal global MOC in the Southern Ocean (SMOC) between 30 and 50 S and 3000 to 4000 m depth (Figure 12, right panel).

The boxplot shows the distribution of the yearly average indices: one for the pre-industrial (black) and two boxes for the first and last 50-year period of each simulation (colors in legend). The AMOC is suppressed at the beginning of the simulations due to the increased forcing, but then slowly recovers, with a final state which is 1-2 Sv stronger (still weaker than pre-industrial). The recovery of the AMOC at multi-centennial timescales has already been discussed (Li et al., 2013; Swingedouw et al., 2007; Lembo et al., 2020) and it has been attributed to various negative feedbacks, including increased northward transport of salinity from the tropical Atlantic (Swingedouw et al., 2007). However, the AMOC is not restored to previous conditions: the circulation increases in strength but becomes shallower, being progressively constrained to the upper region of the ocean, as shown by the decreasing depth of the maximum (Figure S5). In fact, the final global-mean ocean state (Figure 9) is less stratified in the upper region (down to about 1000 m) with respect to the beginning, favouring the recovery of the AMOC (Swingedouw et al., 2007), but more stratified below, due to the fact that the deep water has warmed at a much slower pace. Thus, the AMOC is confined upwards and it is less able to transfer heat to intermediate depths.

The abyssal SMOC cell (Figure 12, right panel) experiences an initial reduction, proportional to forcing, and then completely collapses in all simulations apart from b990. This is relevant since the Southern ocean is a key region for deep ocean heat uptake (Morrison et al., 2016; Gjermundsen et al., 2021), and the reduced ventilation at depth prevents warmer waters to reach the deepest layers, thereby damping the dependence on forcing of the response. The collapse of the abyssal SMOC cell is likely connected to the complete disappearance of deep convection at depths larger than 2000 m in all simulations apart from b990 and b025 (also substantially reduced), following the mechanism proposed by (Gjermundsen et al., 2021).

If the reduced downward heat advection is a plausible candidate to explain the reduced efficiency of the deep ocean heat uptake at higher forcing, it is also likely that changes in other processes are contributing to the heat budget. For example, Morrison et al. (2016) observe that a decrease in the along-isopycnal temperature gradient in warmer climates would reduce the upward heat flux due to eddies and diffusion, thereby increasing the warming at depth. The current understanding of vertical heat fluxes in the deep ocean is still partial and the response is strongly model-dependent, governed by the specific

https://doi.org/10.5194/esd-2023-15
Preprint. Discussion started: 12 May 2023

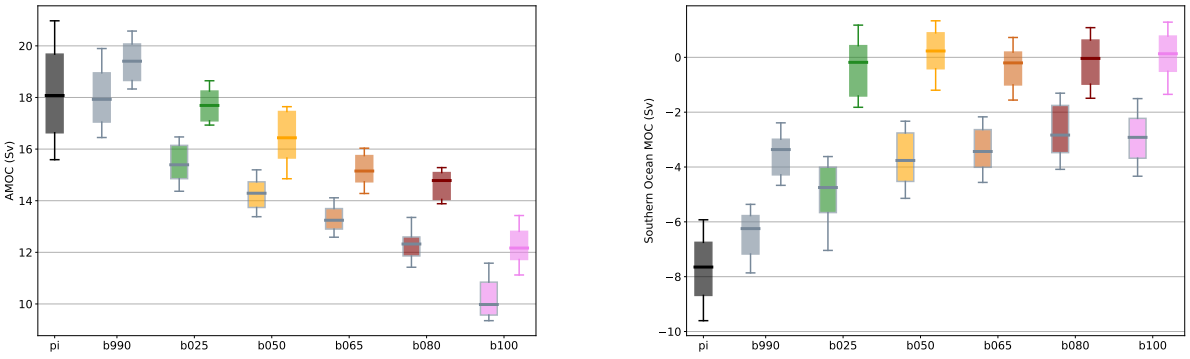

Figure 12. Boxplot of the yearly distribution of AMOC (left panel) and SMOC (right panel) strength at the beginning and end of each simulation (50 yrs).

implementation of eddy and diffusion parametrizations (Exarchou et al., 2015) or by the strength of the deep convection in the model Gjermundsen et al. (2021).

5 Conclusions

We presented here a set of abrupt stabilization simulations performed with EC-Earth3 and analysed the equilibration pathway of the climate system with a focus on the multi-centennial timescales. The six simulations - with external forcing ranging from that of year 1990 (b990) to year 2100 of the SSP5-8.5 scenario (b100) - show a final temperature increase between 1.4 and 9.6 K with respect to pre-industrial. The global GTAS stabilizes in all simulations after 600 to 900 years, apart from b050 which still shows a significant trend at the end of the simulation. The global mean hydrological cycle response intensifies during stabilization, leading to an increased trend per degree of global warming, due to the increased surface energy available for evaporation (Wu et al., 2010). Winter Arctic sea-ice collapses in two simulations (b080, b100), consistent with Meccia et al. (2020), and has apparently reached a tipping point in b065, where the system switches periodically between a low and a high sea-ice cover state.

We then analyzed the evolution of the temperature and precipitation patterns during stabilization (Section 3.2). In all simulations, there is a drastic acceleration of the warming in the Southern Ocean, but the pattern of the response is also dependent on forcing. In particular, at lower forcing the increase is concentrated to the South of the Atlantic and Indian oceans, and extends to the Pacific region only at higher forcing (Figure 6). The precipitation patterns also evolve during stabilization. In general, drying trends found in the sub-tropical oceans and in Mediterranean-like hotspots during SSP5-8.5 tend to reduce during stabilization, or even to reverse. This is generally in line with Zappa et al. (2020), although the inversion of the trend is more clear for larger forcing, especially for the southern subtropics. Also, at large forcing (b100), a strong perturbation is observed in the tropical region, with drying over the West Pacific warm pool and wettening of the Amazon, hinting at significant changes in

https://doi.org/10.5194/esd-2023-15
Preprint. Discussion started: 12 May 2023

the Walker circulation. Even in the regions where the trend inverts during stabilization, the total precipitation change at the end of the simulation with respect of pre-industrial is generally in the same direction as the transient one, but reduced in amplitude.

The multi-centennial timescales of the climate response are driven by the transfer of heat to the deep ocean. We analyzed the heat stored in the upper (0-700 m), mid (700-2000 m) and deep layers of the global ocean in the simulations, and found that the distribution of the heat absorbed in the three layers is strongly dependent on forcing: the heat is almost uniformly distributed along the depth profile in lowest forcing (b990), while in the largest forcing the upper ocean absorbed most of the additional heat. We found that the rate of deep ocean warming is almost independent from the external forcing and the maximum is reached at an intermediate forcing level (b050), meaning that the efficiency of the heat transfer to the deep ocean decreases for larger forcing and at longer timescales. We hypothesize that this is due to a decreased ventilation of the deep ocean with larger forcing. Indeed, the AMOC slightly recovers in intensity during the simulation, but the AMOC cell is shallower and less able to transport heat at depth. At the same time, the abyssal MOC in the Southern ocean is first damped proportionally to forcing and then completely collapses during stabilization, further reducing the mass flux to the deeper layers.

The results highlight the importance of studying multi-centennial timescales of climate change to better understand and constrain processes - first of all, deep ocean heat uptake and the resulting feedback on the surface patterns - that will play a role in determining the final response of the climate system once GHGs concentrations are stabilized.

Data availability. The data of the simulations are available upon request to the corresponding author. Part of the data will be made publicly available in CMOR format through a sharing platform (details will be added here).

Author contributions. FF, PD, SC and GZ planned the simulation setup, PD and FF ported the model code on the HPC machine, FF performed most of the simulations, managed the data produced, and performed most of the data analysis, with feedbacks from all authors. VM run one of the simulations and helped with the AMOC analysis. FF wrote the first draft of the paper; VM, PD, GZ, AB, KB, VL and SC all commented and/or edited the manuscript.

Competing interests. The authors declare no competing interest.

Acknowledgements. The simulations have been performed under the project QUECLIM (Quasi-equilibrium climates at fixed external forcing) at CINECA (IscrB_QUECLIM) and ECMWF (special project spitfab2). KB has received funding from the European Union's Horizon 2020 research and innovation programme under the Marie Sklodowska-Curie grant agreement No. 101026907 (CliMOC).

https://doi.org/10.5194/esd-2023-15
Preprint. Discussion started: 12 May 2023

References

Armour, K. C., Marshall, J., Scott, J. R., Donohoe, A., and Newsom, E. R.: Southern Ocean Warming Delayed by Circumpolar Upwelling and Equatorward Transport, Nature Geoscience, 9, 549–554, https://doi.org/10.1038/ngeo2731, 2016.

Armstrong McKay, D. I., Staal, A., Abrams, J. F., Winkelmann, R., Sakschewski, B., Loriani, S., Fetzer, I., Cornell, S. E., Rockström, J., and Lenton, T. M.: Exceeding 1.5°C Global Warming Could Trigger Multiple Climate Tipping Points, Science, 377, eabn7950, https://doi.org/10.1126/science.abn7950, 2022.

Balsamo, G., Beljaars, A., Scipal, K., Viterbo, P., van den Hurk, B., Hirschi, M., and Betts, A. K.: A Revised Hydrology for the ECMWF Model: Verification from Field Site to Terrestrial Water Storage and Impact in the Integrated Forecast System, Journal of Hydrometeorology, 10, 623–643, https://doi.org/10.1175/2008JHM1068.1, 2009.

Bathiany, S., Notz, D., Mauritsen, T., Raedel, G., and Brovkin, V.: On the Potential for Abrupt Arctic Winter Sea Ice Loss, Journal of Climate, 29, 2703–2719, https://doi.org/10.1175/JCLI-D-15-0466.1, 2016.

Bellomo, K., Angeloni, M., Corti, S., and von Hardenberg, J.: Future Climate Change Shaped by Inter-Model Differences in Atlantic Meridional Overturning Circulation Response, Nature Communications, 12, 3659, https://doi.org/10.1038/s41467-021-24015-w, 2021.

Boé, J., Hall, A., and Qu, X.: Deep Ocean Heat Uptake as a Major Source of Spread in Transient Climate Change Simulations, Geophysical Research Letters, 36, https://doi.org/10.1029/2009GL040845, 2009.

Döscher, R., Acosta, M., Alessandri, A., Anthoni, P., Arsouze, T., Bergman, T., Bernardello, R., Boussetta, S., Caron, L.-P., Carver, G., Castrillo, M., Catalano, F., Cvijanovic, I., Davini, P., Dekker, E., Doblas-Reyes, F. J., Docquier, D., Echevarria, P., Fladrich, U., Fuentes-Franco, R., Gröger, M., v. Hardenberg, J., Hieronymus, J., Karami, M. P., Keskinen, J.-P., Koenigk, T., Makkonen, R., Massonnet, F., Ménégoz, M., Miller, P. A., Moreno-Chamarro, E., Nieradzik, L., van Noije, T., Nolan, P., O'Donnell, D., Ollinaho, P., van den Oord, G., Ortega, P., Prims, O. T., Ramos, A., Reerink, T., Rousset, C., Ruprich-Robert, Y., Le Sager, P., Schmith, T., Schrödner, R., Serva, F., Sicardi, V., Sloth Madsen, M., Smith, B., Tian, T., Tourigny, E., Uotila, P., Vancoppenolle, M., Wang, S., Wårlind, D., Willén, U., Wyser, K., Yang, S., Yepes-Arbós, X., and Zhang, Q.: The EC-Earth3 Earth System Model for the Coupled Model Intercomparison Project 6, Geoscientific Model Development, 15, 2973–3020, https://doi.org/10.5194/gmd-15-2973-2022, 2022.

Drijfhout, S., Bathiany, S., Beaulieu, C., Brovkin, V., Claussen, M., Huntingford, C., Scheffer, M., Sgubin, G., and Swingedouw, D.: Catalogue of Abrupt Shifts in Intergovernmental Panel on Climate Change Climate Models, Proceedings of the National Academy of Sciences, 112, E5777–E5786, https://doi.org/10.1073/pnas.1511451112, 2015.

Exarchou, E., Kuhlbrodt, T., Gregory, J. M., and Smith, R. S.: Ocean Heat Uptake Processes: A Model Intercomparison, Journal of Climate, 28, 887–908, https://doi.org/10.1175/JCLI-D-14-00235.1, 2015.

Eyring, V., Bony, S., Meehl, G. A., Senior, C. A., Stevens, B., Stouffer, R. J., and Taylor, K. E.: Overview of the Coupled Model Intercomparison Project Phase 6 (CMIP6) Experimental Design and Organization, Geoscientific Model Development, 9, 1937–1958, 2016.

Fichefet, T. and Maqueda, M. A. M.: Sensitivity of a Global Sea Ice Model to the Treatment of Ice Thermodynamics and Dynamics, Journal of Geophysical Research: Oceans, 102, 12 609–12 646, https://doi.org/10.1029/97JC00480, 1997.

Fiedler, S., Stevens, B., Gidden, M., Smith, S. J., Riahi, K., and van Vuuren, D.: First Forcing Estimates from the Future CMIP6 Scenarios of Anthropogenic Aerosol Optical Properties and an Associated Twomey Effect, Geoscientific Model Development, 12, 989–1007, https://doi.org/10.5194/gmd-12-989-2019, 2019.

Gidden, M. J., Riahi, K., Smith, S. J., Fujimori, S., Luderer, G., Kriegler, E., van Vuuren, D. P., van den Berg, M., Feng, L., Klein, D., Calvin, K., Doelman, J. C., Frank, S., Fricko, O., Harmsen, M., Hasegawa, T., Havlik, P., Hilaire, J., Hoesly, R., Horing, J., Popp, A., Stehfest, E.,

https://doi.org/10.5194/esd-2023-15
Preprint. Discussion started: 12 May 2023

and Takahashi, K.: Global Emissions Pathways under Different Socioeconomic Scenarios for Use in CMIP6: A Dataset of Harmonized Emissions Trajectories through the End of the Century, Geoscientific Model Development, 12, 1443–1475, https://doi.org/10.5194/gmd-12-1443-2019, 2019.

Gjermundsen, A., Nummelin, A., Olivié, D., Bentsen, M., Seland, Ø., and Schulz, M.: Shutdown of Southern Ocean Convection Controls Long-Term Greenhouse Gas-Induced Warming, Nature Geoscience, 14, 724–731, https://doi.org/10.1038/s41561-021-00825-x, 2021.

Gregory, J. M.: Vertical Heat Transports in the Ocean and Their Effect on Time-Dependent Climate Change, Climate Dynamics, 16, 501–515, https://doi.org/10.1007/s003820000059, 2000.

He, J. and Soden, B. J.: A Re-Examination of the Projected Subtropical Precipitation Decline, Nature Climate Change, 7, 53–57, https://doi.org/10.1038/nclimate3157, 2017.

Hieronymus, M. and Nycander, J.: The Budgets of Heat and Salinity in NEMO, Ocean Modelling, 67, 28–38, https://doi.org/10.1016/j.ocemod.2013.03.006, 2013.

Jones, C. D., Frölicher, T. L., Koven, C., MacDougall, A. H., Matthews, H. D., Zickfeld, K., Rogelj, J., Tokarska, K. B., Gillett, N. P., Ilyina, T., Meinshausen, M., Mengis, N., Séférian, R., Eby, M., and Burger, F. A.: The Zero Emissions Commitment Model Intercomparison Project (ZECMIP) Contribution to C4MIP: Quantifying Committed Climate Changes Following Zero Carbon Emissions, Geoscientific Model Development, 12, 4375–4385, https://doi.org/10.5194/gmd-12-4375-2019, 2019.

King, A. D., Lane, T. P., Henley, B. J., and Brown, J. R.: Global and Regional Impacts Differ between Transient and Equilibrium Warmer Worlds, Nature Climate Change, 10, 42–47, https://doi.org/10.1038/s41558-019-0658-7, 2020.

Knutti, R., Rugenstein, M. A. A., and Hegerl, G. C.: Beyond Equilibrium Climate Sensitivity, Nature Geoscience, 10, 727–736, https://doi.org/10.1038/ngeo3017, 2017.

Kostov, Y., Armour, K. C., and Marshall, J.: Impact of the Atlantic Meridional Overturning Circulation on Ocean Heat Storage and Transient Climate Change, Geophysical Research Letters, 41, 2108–2116, https://doi.org/10.1002/2013GL058998, 2014.

Lee, J.-Y., Marotzke, J., Bala, G., Cao, L., Corti, S., Dunne, J. P., Engelbrecht, F., Fischer, E., Fyfe, J. C., Jones, C., Maycock, A., Mutemi, J., Ndiaye, O., Panickal, S., and Zhou, T.: Future Global Climate: Scenario-Based Projections and near-Term Information, in: Climate Change 2021: The Physical Science Basis. Contribution of Working Group I to the Sixth Assessment Report of the Intergovernmental Panel on Climate Change, edited by Masson-Delmotte, V., Zhai, P., Pirani, A., Connors, S. L., Péan, C., Berger, S., Caud, N., Chen, Y., Goldfarb, L., Gomis, M. I., Huang, M., Leitzell, K., Lonnoy, E., Matthews, J. B. R., Maycock, T. K., Waterfield, T., Yelekçi, Ö., Yu, R., and Zhou, B., pp. 553–672, Cambridge University Press, Cambridge, United Kingdom and New York, NY, USA, https://doi.org/10.1017/9781009157896.001, 2021.

Lembo, V., Lucarini, V., and Ragone, F.: Beyond Forcing Scenarios: Predicting Climate Change through Response Operators in a Coupled General Circulation Model, Scientific Reports, 10, 8668, https://doi.org/10.1038/s41598-020-65297-2, 2020.

Lenton, T. M., Rockström, J., Gaffney, O., Rahmstorf, S., Richardson, K., Steffen, W., and Schellnhuber, H. J.: Climate Tipping Points — Too Risky to Bet Against, Nature, 575, 592–595, https://doi.org/10.1038/d41586-019-03595-0, 2019.

Li, C., von Storch, J.-S., and Marotzke, J.: Deep-Ocean Heat Uptake and Equilibrium Climate Response, Climate Dynamics, 40, 1071–1086, https://doi.org/10.1007/s00382-012-1350-z, 2013.

Madec, G.: NEMO Ocean Engine: Note Du Pole de Modélisation, Institut Pierre-Simon Laplace (IPSL), France, No 27 ISSN No 1288-1619, Technical ReportTech. Rep, 2008.

McDougall, T. J.: Potential Enthalpy: A Conservative Oceanic Variable for Evaluating Heat Content and Heat Fluxes, Journal of Physical Oceanography, 33, 945–963, https://doi.org/10.1175/1520-0485(2003)033<0945:PEACOV>2.0.CO;2, 2003.

https://doi.org/10.5194/esd-2023-15
Preprint. Discussion started: 12 May 2023

Meccia, V. L., Fabiano, F., Davini, P., and Corti, S.: Stochastic Parameterizations and the Climate Response to External Forcing: An Experiment With EC-Earth, Geophysical Research Letters, 47, e2019GL085 951, https://doi.org/10.1029/2019GL085951, 2020.

Meccia, V. L., Fuentes-Franco, R., Davini, P., Bellomo, K., Fabiano, F., Yang, S., and von Hardenberg, J.: Internal Multi-Centennial Variability of the Atlantic Meridional Overturning Circulation Simulated by EC-Earth3, Climate Dynamics, https://doi.org/10.1007/s00382-022-06534-4, 2022.

Morrison, A. K., Griffies, S. M., Winton, M., Anderson, W. G., and Sarmiento, J. L.: Mechanisms of Southern Ocean Heat Uptake and Transport in a Global Eddying Climate Model, Journal of Climate, 29, 2059–2075, https://doi.org/10.1175/JCLI-D-15-0579.1, 2016.

O'Neill, B. C., Tebaldi, C., van Vuuren, D. P., Eyring, V., Friedlingstein, P., Hurtt, G., Knutti, R., Kriegler, E., Lamarque, J.-F., Lowe, J., Meehl, G. A., Moss, R., Riahi, K., and Sanderson, B. M.: The Scenario Model Intercomparison Project (ScenarioMIP) for CMIP6, Geoscientific Model Development, 9, 3461–3482, https://doi.org/10.5194/gmd-9-3461-2016, 2016.

Rugenstein, M., Bloch-Johnson, J., Abe-Ouchi, A., Andrews, T., Beyerle, U., Cao, L., Chadha, T., Danabasoglu, G., Dufresne, J.-L., Duan, L., Foujols, M.-A., Frölicher, T., Geoffroy, O., Gregory, J., Knutti, R., Li, C., Marzocchi, A., Mauritsen, T., Menary, M., Moyer, E., Nazarenko, L., Paynter, D., Saint-Martin, D., Schmidt, G. A., Yamamoto, A., and Yang, S.: LongRunMIP: Motivation and Design for a Large Collection of Millennial-Length AOGCM Simulations, Bulletin of the American Meteorological Society, 100, 2551–2570, https://doi.org/10.1175/BAMS-D-19-0068.1, 2019.

Samset, B. H., Myhre, G., Forster, P. M., Hodnebrog, Ø., Andrews, T., Faluvegi, G., Fläschner, D., Kasoar, M., Kharin, V., Kirkevåg, A., Lamarque, J.-F., Olivié, D., Richardson, T., Shindell, D., Shine, K. P., Takemura, T., and Voulgarakis, A.: Fast and Slow Precipitation Responses to Individual Climate Forcers: A PDRMIP Multimodel Study, Geophysical Research Letters, 43, 2782–2791, https://doi.org/10.1002/2016GL068064, 2016.

Stevens, B., Fiedler, S., Kinne, S., Peters, K., Rast, S., Müsse, J., Smith, S. J., and Mauritsen, T.: MACv2-SP: A Parameterization of Anthropogenic Aerosol Optical Properties and an Associated Twomey Effect for Use in CMIP6, Geoscientific Model Development, 10, 433–452, https://doi.org/10.5194/gmd-10-433-2017, 2017.

Swingedouw, D., Braconnot, P., Delecluse, P., Guilyardi, E., and Marti, O.: Quantifying the AMOC Feedbacks during a 2×CO2 Stabilization Experiment with Land-Ice Melting, Climate Dynamics, 29, 521–534, https://doi.org/10.1007/s00382-007-0250-0, 2007.

Wu, P., Wood, R., Ridley, J., and Lowe, J.: Temporary Acceleration of the Hydrological Cycle in Response to a CO2 Rampdown, Geophysical Research Letters, 37, https://doi.org/10.1029/2010GL043730, 2010.

Zappa, G., Ceppi, P., and Shepherd, T. G.: Time-Evolving Sea-Surface Warming Patterns Modulate the Climate Change Response of Subtropical Precipitation over Land, Proceedings of the National Academy of Sciences, 117, 4539–4545, https://doi.org/10.1073/pnas.1911015117, 2020.

Zickfeld, K., Eby, M., Weaver, A. J., Alexander, K., Crespin, E., Edwards, N. R., Eliseev, A. V., Feulner, G., Fichefet, T., Forest, C. E., Friedlingstein, P., Goosse, H., Holden, P. B., Joos, F., Kawamiya, M., Kicklighter, D., Kienert, H., Matsumoto, K., Mokhov, I. I., Monier, E., Olsen, S. M., Pedersen, J. O. P., Perrette, M., Philippon-Berthier, G., Ridgwell, A., Schlosser, A., Deimling, T. S. V., Shaffer, G., Sokolov, A., Spahni, R., Steinacher, M., Tachiiri, K., Tokos, K. S., Yoshimori, M., Zeng, N., and Zhao, F.: Long-Term Climate Change Commitment and Reversibility: An EMIC Intercomparison, Journal of Climate, 26, 5782–5809, https://doi.org/10.1175/JCLI-D-12-00584.1, 2013.